Journal of Neuroscience Research 86:1520–1528 (2008)

Early Postnatal Development of Rat Brain: In Vivo Diffusion Tensor Imaging

K.H. Bockhorst,[1] P.A. Narayana,[1]* R. Liu,[2] P. Ahobila-Vijjula,[1] J. Ramu,[1] M. Kamel,[2] J. Wosik,[2] T. Bockhorst,[1] K. Hahn,[3] K.M. Hasan,[1] and J.R. Perez-Polo[4]

[1]University of Texas at Houston, Houston, Texas
[2]University of Houston, Houston, Texas
[3]GSF-National Research Center for Environment and Health, Neuherberg, Germany
[4]University of Texas Medical Branch, Galveston, Texas

Perinatal hypoxia is a major cause of neurodevelopmental deficits. Neuronal migration patterns are particularly sensitive to perinatal hypoxia/ischemia and are associated with the clinical deficits. The rat model of hypoxia/ischemia at P7 mimics that of perinatal injury in humans. Before assessing the effects of postnatal injury on brain development, it is essential to determine the normal developmental trajectories of various brain structures in individual animals. In vivo longitudinal diffusion tensor imaging (DTI) was performed from postnatal day 0 (P0) to P56 on Wistar rats. The DTI metrics, mean diffusivity (MD), fractional anisotropy (FA), axial (λl) and radial (λt) diffusivities, were determined for four gray matter and eight white matter structures. The FA of the cortical plate and the body of corpus callosum decreased significantly during the first 3 weeks after birth. The decrease in the cortical plate's FA value was associated mainly with an increase in λt. The initial decrease in FA of corpus callosum was associated with a significant decrease in λl. The FA of corpus callosum increased during the rest of the observational period, which was mainly associated with a decrease in λt. The FA of gray matter structures, hippocampus, caudate putamen, and cortical mantle did not show significant changes between P0 and P56. In contrast, the majority of white matter structures showed significant changes between P0 and P56. These temporal changes in the DTI metrics were related to the neuronal and axonal pruning and myelination that are known to occur in the developing brain.

Key words: hypoxia; diffusion tensor imaging; brain development

Prenatal and perinatal hypoxia is a major cause of neurodevelopmental deficits and the resultant motor, behavioral, and cognitive outcomes. Moreover, perinatal hypoxia is frequently associated with epilepsy (Arpino et al., 2001; Toet et al., 2005). To develop rational therapeutic strategies, it is necessary to characterize the perturbations in brain development associated with perinatal hypoxia/ischemia. Specifically, those developmental changes, including neuronal migration, that are associated with deficits present in the patient population over time (Rice and Barone, 2000). One useful model is the rat P7 model of hypoxia/ischemia that is commonly employed to study the effects of variety of perinatal brain injuries (Vannucci et al., 1999; Hagberg et al., 2002). For example, brain development at P7 in rats is comparable to that of premature or full-term infants (Vannucci et al., 1999; Hagberg et al., 2002). For example, hypoxic injury at P7 in the rat is considered a model of cerebral palsy (Qiao et al., 2004). Thus, perinatal brain injury in rodents mimics that of prenatal injury in humans. Thus, longitudinal characterization of brain development during the early postnatal period in rats has considerable significance in terms of prenatal brain injury in humans. However, before assessing the effects of postnatal injury on brain development, it is essential to determine the normal developmental trajectories of various brain structures in individual animals.

Diffusion tensor imaging (DTI) is a powerful technique for probing the microstructural organization of brain tissue (Mori and Zhang, 2006). DTI has been employed by a number of groups to follow brain development in rodents (Mori et al., 2001; Zhang et al., 2003, 2005; Verma et al., 2005; Chahboune et al., 2007; Huang et al., 2007; Larvaron et al., 2007; Sizonenko et al., 2007). However, most of these studies were performed on ex vivo brains. As summarized in Table I, published quantitative values of fractional anisotropy (FA), a measure of diffusion anisotropy that is used to infer the developmental trajectory of brain, greatly differ from study to study, sometimes even from the same group (Verma et al., 2005; Zhang et al., 2006). The dif-

Contract grant sponsor: NIH; Contract grant number: 5P01HD039833 (to J.R.P.-P.).

*Correspondence to: P.A. Narayana, University of Texas at Houston, Houston, TX 77030. E-mail: ponnada.a.narayana@uth.tmc.edu

Received 10 August 2007; Revised 23 October 2007; Accepted 24 October 2007

Published online 11 January 2008 in Wiley InterScience (www.interscience.wiley.com). DOI: 10.1002/jnr.21607

TABLE I. Summary of the Published DTI Results in Rodents*

Reference	Species	Mode	Time points (total number)	Diffusion gradients	Brain structures	FA bcc	FA scc	FA gcc	FA cp	FA cm
Boretius et al., 2004	r, m	i	u (1)	6	2	7	–	–	–	–
Chahboune et al., 2007	m	i	P15–45 (4)	16	5	0.60 (P45)	–	–	∼0.16[a] (P45)	∼0.16[a] (P45)
Guilfoyle et al., 2003	m	i, e	u (1)	6	1	0.75 0.78	–	–	–	–
Larvaron et al., 2007	m	i	P5–54 (4)	6	9	–	0.79	0.73	0.38[a]	0.38[a]
Lee et al., 2006	r	i	a (1)	32	2	0.32	–	–	–	–
Mayer et al., 2007	r	i	P90, P240 (2)	6	2	–	0.45[b]	0.42[b]	–	–
Numano et al., 2006	r	i	P126 (1)	6	3	0.50	–	–	0.26[a]	0.26[a]
Sizonenko et al., 2007	r	i	P3, P6 (2)	6	2	–	–	–	0.36	0.21
Verma et al., 2005	m	e	P2–80[b] (3)	6	14	–	∼0.38	∼0.32	∼0.11	∼0.12
Nair et al., 2005	r	i	P56–70[b] (1)	6	1	0.52	–	–	–	–
Xue et al., 1999	r	i	a (1)	6	2	–	–	–	–	–
Zhang et al., 2006	m	e	E13–a (6)	6	7	0.80[a] (a)	–	–	∼0.15[a]	∼0.15[a] (a)
Zhang et al., 2002	m	e	a (1)	6	2	–	–	–	–	–

*r, rat; m, mouse; i, in vivo; e, ex vivo; u, unknown; a, adult.
[a]No differentiation between cortical plate (cp) or mantle (cm).
[b]Average; a, adult; u, unknown; bcc, scc, gcc, body, splenium, and genu of corpus callosum.

ferent tissue fixation techniques with the variable intervals between the fixation and DTI studies could explain some of the differing results. As pointed out by Huang et al. (2006), although post-mortem-based studies are highly useful for morphological description of anatomy, they are probably not reliable for quantification of MRI metrics such as spin-spin relaxation (T2), spin-lattice relaxation time (T1), FA, and mean diffusivity (MD) values. It is, therefore, important to measure the temporal changes in diffusion anisotropy in live animals to minimize these artifacts.

Temporal changes in the diffusion anisotropy in vivo have been recently reported for rodents by Chahboune et al. (2007), Larvaron et al. (2007), and Sizonenko et al. (2007). These studies were performed at a relatively few time points (n = 4) and may not be adequate to define the developmental trajectory. In addition, these studies focused on a few brain structures. Again, as shown in Table I, the measured values differed among different studies. Most DTI studies in rodent brain development focused on mice. However, rats are more commonly used as animal models to study prenatal hypoxic ischemic injury (Rice et al., 1981; Fabian et al., 2007), and in vivo studies that document the development of rat brain at early perinatal age are not available.

In these studies, we measured in vivo DTI metrics of various gray matter and white matter structures in Wistar rats at 10 time points from P0 (day of birth) to P56. The measured temporal changes in the DTI metrics were related to neuronal and axonal pruning and myelination that are known to occur in the developing brain.

MATERIALS AND METHODS

Animals

Pregnant Wistar rats were shipped to our facility 1 week prior to expected delivery. The litters were culled to 10 pups. The pups stayed with the mother until they were weaned at the age of 4 weeks or later. MRI studies were performed on 44 rats, on postnatal days 0, 2, 4, 6, 8, 14, 21, 28, 42, and 56. The numbers of animals included at each time point were six at P6, five at P28 and P56, and four at all other time points.

MRI Protocol

All MRI scans were performed on a 7T Bruker Biospec horizontal bore scanner (USR70/30; Bruker, Karlsruhe, Germany) with a S116 gradient insert that can produce a maximal gradient amplitude of 400 mT/m with a settling time of less than 80 μsec. A 72-mm-inner-diameter volume coil supplied by Bruker was used for radiofrequency (RF) transmission. For improved signal-to-noise ratio (SNR), a custom-designed 22-mm-outer-diameter circular surface coil was used for signal reception. This coil consists of two split rings placed on two sides of a dielectric substrate (RT/Duroid 5870; Rogers Co., Chandler, AZ) to minimize the stray electric fields. The rings were rotated 180° with respect to each other. This design avoided additional dielectric losses resulting from coupling between the electric field and the tissue (Kamel et al., 2007).

Animals were initially anesthetized with 4% isofluorane and an air/oxygen mixture (7:3). The isofluorane level was lowered to 2.0% ± 0.5% during the magnetic resonance imaging (MRI) scans. Because of the small size, the heads of animals younger than 4 weeks were placed in a custom-built tube-shaped mask (∼13 mm outer diameter), which was connected to the anesthesia system (ventilator: Inspira asv, Harvard Apparatus, Holliston, MA; vaporizer: VMS Anesthesia Machine, MDS Matrix, Orchard Park, NY). Older animals' (>4 weeks) heads were fixed in a commercial holder (Bruker) using ear and tooth bars. Throughout the MRI scan, the animal's body temperature was kept at 36°C ± 1°C with a feedback-controlled warm air system (SA Instruments, Stony Brook, NY). The respiration and rectal (for older animals) or surface body temperature (for younger animals) were continuously monitored with a small-animal monitoring system (SA Instruments). Young animals weigh only a few grams and have not yet not developed a bony skull. Therefore, after an exposure of about 1 hr to a flow of warm air, it is reasonable

to assume that the core temperature of the brain does not significantly differ from the surface temperature. For older animals, the rectal temperature is shown to correlate strongly with the core temperature (Eshraghi et al., 2005; Greer et al., 2007). The oxygen level and heart rate were monitored with an MRI-compatible pulse oximeter (NONIN, Plymouth, MN). The average time for which animals were under anesthesia for MRI was less than 2 hr. The animals woke up within 10 min after turning off the anesthesia. The survival rate of animals in these studies was about 95%.

Anatomical images. Following the tripilot scan, "Fastmap" (ParaVision; Bruker), an automatic magnetic field shimming procedure, was used to maximize the magnetic field homogeneity over a 15 mm × 15 mm × 15 mm cube. The power levels of the RF excitation pulses and the receiver gain were manually adjusted. Multislice, contiguous coronal images were acquired with dual-echo rapid acquisition and relaxation enhancement (RARE) sequence with the following parameters: TE1/TE2/TR = 22 msec/66 msec/5,000 msec, where TE1 and TE2 are the echo times and TR is the repetition time; RARE factor = 4; slice thickness = 0.5 mm; square field of view (FOV) = 35 mm; acquisition matrix = 256 × 192, which was zero filled to 256 × 256. The number of slices was between 20 and 40, depending on the size of the brain.

Diffusion-weighted imaging. Diffusion-weighted imaging (DWI) data were acquired with a four-shot spin-echo EPI sequence with geometry and location identical to those of the RARE scan. A rotationally invariant icosahedral encoding scheme with 21 alternating polarity encoding directions (total number of encoding directions, N_e = 42; Madi et al., 2005) with a diffusion sensitization or b-factor of either 700 or 1,050 sec/mm^2 was used to acquire DWI. The relatively high MD in pups results in poor SNR at high b-factor values. Therefore, a lower b value was used for imaging pups. The acquisition parameters were: TE/TR = 38 msec/4,000 msec; diffusion gradient pulse duration, δ, = 2.3 msec; gradient separation, Δ = 22 msec, sweep width = 200 kHz; acquisition matrix = 128 × 128, spatial resolution of 0.27 mm × 0.27 mm × 0.5 mm, number of repetitions = 9 with b = 0 (reference or b0 images), number of repetitions = 4 with diffusion-weighting per encoding direction. Navigator echoes were used to correct for the ghost artifacts. Each scan resulted in up to 8,800 images. The average acquisition time was 35 min.

As a part of our quality assurance (QA) program, we regularly evaluate the performance of our system using DTI measurements on water phantoms. As described elsewhere, this regular QA program ensures excellent spatial and temporal stability of our DTI measures (Madi et al., 2005).

Data processing. All the data processing was performed on a PC (Dell Pentium 4, 3 GHz, 2 GB RAM) operating under Windows XP. A custom-made program written in IDL (ITTVis, Boulder, CO) automatically identified and eliminated images with significant ghosting. The images were magnitude-averaged and automatically cropped to a 71 × 71 matrix for reducing the amount of data processing. The data were filtered, followed by a Rician bias correction (Hahn et al., 2004, 2005). Extrameningeal tissues were manually cropped in ImageJ (NIH, Bethesda, MD) for a set of images acquired with one gradient encoding direction. This mask was applied to images acquired with all other encoding directions and to the b0 images for brain extraction. The diffusion-weighted images were warped to the corresponding b0 images using AIR (align_warp, 3D, model 2; Woods et al., 1998a,b) for minimizing the image distortions by the eddy currents induced by strong diffusion gradients. All the above-mentioned processing steps (except the manual stripping of extrameningeal tissue) were fully automatic and were processed as batch jobs.

The mean diffusivity (MD), axial (λl) and radial (λt) eigenvalues (or diffusivities), and FA maps were generated from the preprocessed DWI data sets using the DTI toolbox (Hasan et al., 2004, 2005). Because the axial and radial diffusivities (or eigenvalues) are shown to provide more specific information about the microstructural environment than FA alone (Song et al., 2002; Deo et al., 2006), we have calculated both λl and λt using the procedure described elsewhere (Hasan and Narayana, 2006). The DTI parameters of various structures were measured using the "ROI manager," which is a part of ImageJ. This allowed the measurements of identical sets of ROIs in the parametric maps. The results were imported into Excel spreadsheets. Statistical analysis (ANOVA, $P < 0.05$, Scheffe's test, if not indicated otherwise) was performed with Intercooled Stata 9 software (StataCorp, College Station, TX).

The measurements included four gray matter structures: hippocampus (hi), caudate putamen (cpu), cortical plate (cp), cortical mantle (cm), and eight white matter structures: body (bcc), genu (gcc), and splenium (scc) of corpus callosum (cc), external (ec) and internal capsule (ic), fimbria (fi), anterior commisure (ac), and cingulum (cg). Data were collected from three slices, which included the scc, or fi, ic, and bcc, or gcc. All the structures were identified by comparing both anatomical images and FA maps with the Paxinos and Watson (2005) atlas. Measurements were performed in each hemisphere, except for structures located at the midline (bcc, scc, and gcc). Measurements of the cortical mantle (close to the external capsule) and the cortical plate (close to the dura) were performed on all three slices in each hemisphere. We did not observe significant differences in the parameters from the homologous structures from individual hemispheres, so these parameters were averaged over the two hemispheres. The FA, MD, λl, and λt values were measured from a total of 98 ROIs for each animal.

RESULTS

Figure 1 displays the FA maps modulated by the principal eigenvector in the coronal plane from P0 to P56. In these color-coded maps blue, green, and red represent caudal-rostral, dorsal-ventral, and left-right directions, respectively. Consistent with the published studies, the cortical plate showed high anisotropy in pups (McKinstry et al., 2002; Gupta et al., 2005; Verma et al., 2005; Zhang et al., 2006; Mori and Zhang, 2006; Sizonenko et al., 2007). The color-coded FA maps clearly demonstrate the radial orientation of the cortical microstructure (Fig. 1). The highest contrast between cp

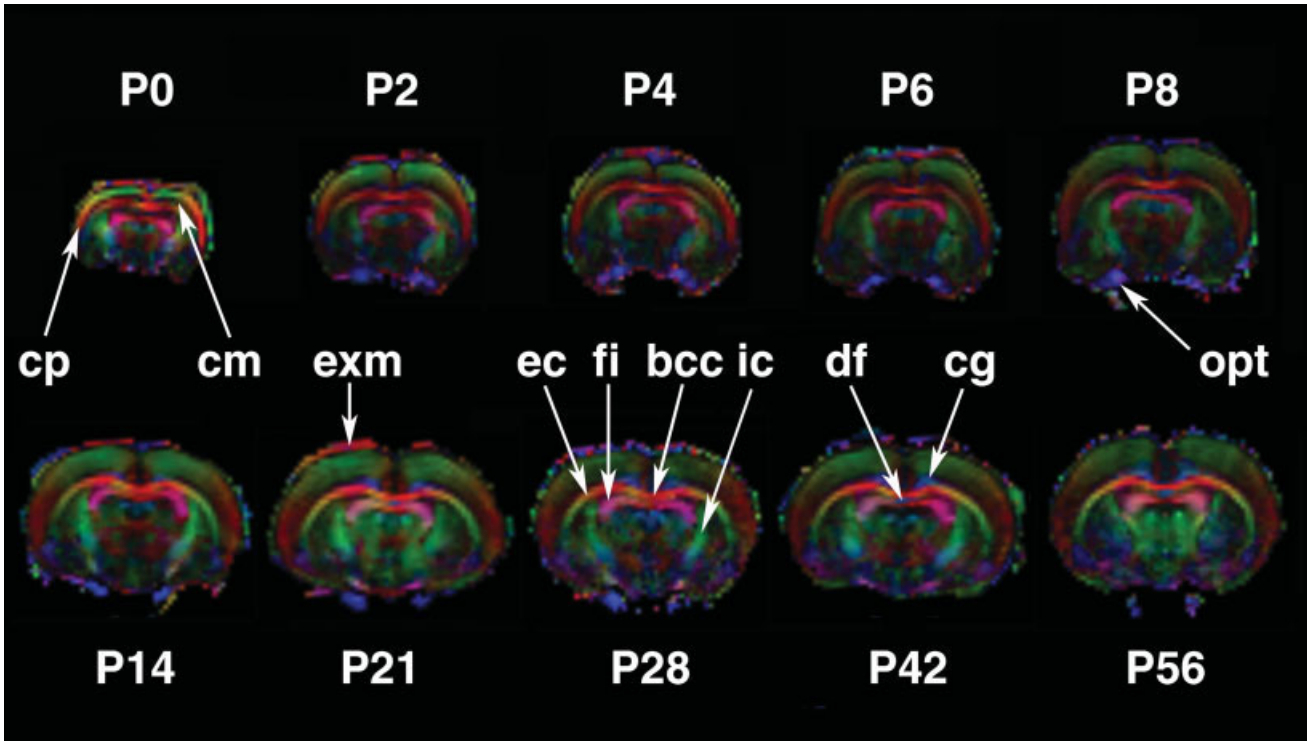

Fig. 1. RGB-FA maps of rat brain from P0 (top left) to P56 (bottom right). The FA maps are color coded to indicate the orientation of the anisotropy: blue, caudal-rostral; red, left-right; and green, dorsal ventral. Highest contrast between cp and cm is observed at P0. Also, note the radial orientation of the cortex: topical segments appear green, parietal segments red. The ec and bcc display a tangential orientation (P28). opt (P8), df, and cg (P42) are coded blue, indicating their caudal-rostral orientation. cg And df became visible 2 weeks after birth. exm indicates the extrameningeal tissue and is the result of imperfect stripping.

TABLE II. DTI Parameters in Different Structures at Days P0 (left) and P56 (right)[†]

	FA × 1,000		MD ($\times 10^{-6}$ mm^2/sec)		λl ($\times 10^{-6}$ mm^2/sec)		λt ($\times 10^{-6}$ mn^2/sec)	
Structure	P0	P56	P0	P56	P0	P56	P0	P56
gcc	582 ± 104	855 ± 41★	1,025 ± 111	846 ± 24	1,958 ± 98	2,018 ± 79	689 ± 155	314 ± 95★
scc	692 ± 90	822 ± 42★	917 ± 253	904 ± 21	2,020 ± 324	2,069 ± 136	507 ± 59	320 ± 50★
fi	605 ± 20	784 ± 74	898 ± 247	929 ± 50	1,786 ± 217	2,057 ± 80	591 ± 48	364 ± 92
ac	392 ± 90	708 ± 59★	718 ± 65	759 ± 35	1,198 ± 315	1,564 ± 100	597 ± 58	402 ± 67★
ic	500 ± 93	681 ± 55★	944 ± 245	783 ± 34	1,547 ± 161	1,703 ± 310	694 ± 54	400 ± 74★
bcc	628 ± 67	676 ± 95	948 ± 212	810 ± 73	1,927 ± 284	1,509 ± 190	593 ± 52	459 ± 67
Ec	469 ± 59	623 ± 122	1,061 ± 236	845 ± 23	1,779 ± 289	1,507 ± 240	793 ± 120	514 ± 109
Cg	236 ± 35	423 ± 16★	1,145 ± 161	791 ± 21★	1,505 ± 138	1,192 ± 34	1,017 ± 82	595 ± 8★
Cp	531 ± 17	286 ± 22★	799 ± 206	738 ± 52	1,450 ± 102	978 ± 45★	576 ± 64	606 ± 74
Cm	169 ± 15	134 ± 14	1,067 ± 130	772 ± 17★	1,291 ± 64	896 ± 20★	987 ± 82	699 ± 37★
Cpu	117 ± 33	123 ± 22	1,278 ± 345	758 ± 33★	1,466 ± 342	861 ± 47★	1,223 ± 331	712 ± 17★
Hi	108 ± 13	119 ± 25	1,174 ± 221	788 ± 24★	1,336 ± 202	900 ± 26★	1,119 ± 192	731 ± 26★

[†]The FA values of most white matter structures and the cortical plate were significantly different.
★Significant difference between P0 and P56. All statistical tests were performed over the complete data set using ANOVA with Scheffe's post hoc test ($P < 0.05$).

and cm occurred at P0 but was still present even at P56. The optical tracts (opt; shown at P8 in Fig. 1), dorsal fornix, and cingulum (df and cg, shown at P42 in Fig. 1) are oriented in the rostral-caudal directions and consequently appear blue in the color-coded maps. The optic tracts were not visible until P2 (Fig. 1). Both cg and df were clearly visible in the second week. The small sizes of opt and df prevented reliable measurements of the DTI metrics in these two structures. The ec, fi, cc, and ic were visible at P0 and continued to be visible with greater prominence during the entire study period (P28; Fig. 1).

Table II summarizes the FA, MD, λl, and λt values at P0 (left column) and P56 (right column). The tempo-

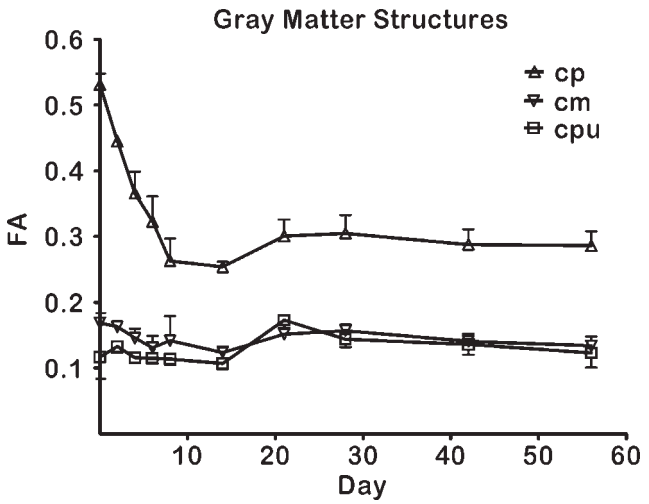

Fig. 2. Temporal changes in the FA values of gray matter structures. The FA of cp (△) decreased significantly during the first week (P0: 0.531 ± 0.017; P14: 0.254 ± 0.008). The FA of cp remained at a level of 0.3 after a significant increase between P14 and P21 (0.301 ± 0.008; $P = 0.0291$). The FA of cm (▽) and cpu (□) did not show significant changes during the observation period.

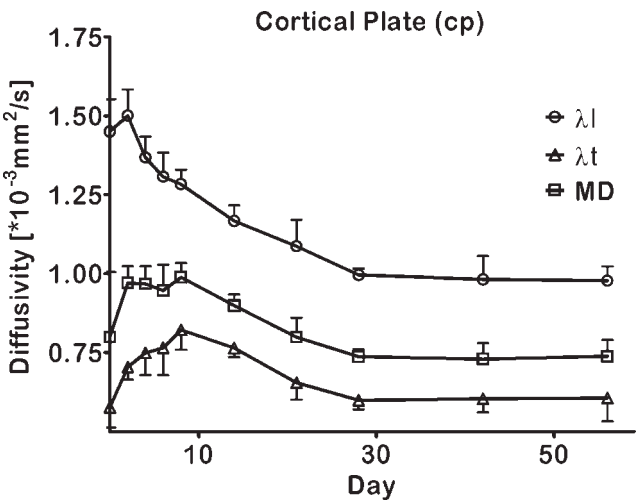

Fig. 3. Temporal changes in the diffusivities in cp. The decreased FA (Fig. 2, △) appears to be mainly associated with an increase in λt (△) between P0 and P8 and paralleled the decrease in λl (○). As a result, MD remained unchanged between P2 and P8, followed by a decrease up to P28. This behavior of MD is typical for all other gray and white matter structures.

ral changes in the DTI metrics were observed to be dependent on the spatial location of the brain structure. In general, the FA increased and MD decreased monotonically with age. However, as described below, not all structures exhibited a monotonic behavior.

Gray Matter Structures

The FA of cortical plate at P0 showed the largest value among all the gray matter structures (0.531 ± 0.017). Its value reached a minimum of 0.254 ± 0.008 (P0 vs. P14; $P < 0.0001$) at P14 and thereafter continued to increase and reached an asymptotic value of 0.286 ± 0.022 ($P = 0.0291$; P14 vs. P56; Fig. 2). As shown in Figure 3, the temporal changes in λt of cp were observed to be nonmonotonic. λt Increased significantly from P0 ($0.576 \pm 0.064 \times 10^{-3}$ mm^2/sec) to P8 ($0.822 \pm 0.062 \times 10^{-3}$ mm^2/sec; $P = 0.009$) with a subsequent steady and significant decrease up to P28 ($0.599 \pm 0.029 \times 10^{-3}$ mm^2/sec; $P = 0.015$) and stayed constant thereafter ($P = 1.000$; P28 vs. P56,). In contrast, λl showed a steady and significant decrease from P0 (1.450 ± 0.083 mm^2/sec) to P28 ($0.978 \pm 0.045 \times 10^{-3}$ mm^2/sec; $P < 0.001$) and stayed constant over the remaining observational period (P28 vs. P56, $P = 0.753$; Fig. 3). The MD of the cortical plate showed no significant changes between P0 and P8 ($0.799 \pm 0.206 \times 10^{-3}$ mm^2/sec; $P = 0.361$) and was followed by a significant decrease up to P28 ($P = 0.043$) that reached a steady value at later time points ($P = 1.000$; P28 vs. P56).

As can be seen in Figure 2, the FA values of cortical mantle, caudate putamen, and hippocampus (not shown to reduce the clutter in the figure) essentially remained the same from P0 to P56 ($P \geq 0.381$). The value of λt of all these three structures decreased significantly with age up to P21 ($P \leq 0.001$) and remained constant over the rest of the observational period ($P > 0.995$; P21 vs. P56). Both MD and λl for all these three structures decreased significantly from P0 to P21 ($P \leq 0.033$) and stayed constant afterwards ($P \geq 0.968$; P21 vs. P56).

White Matter Structures

Corpus callosum. The temporal changes in the DTI metrics were observed to be different for different parts of corpus callosum (Fig. 4). The FA value of the body of the corpus callosum (bcc) showed a rapid decrease from P0 (0.628 ± 0.067; $P = 0.03$) and reached a minimum at P21 (0.444 ± 0.044). After P21, it steadily and significantly increased up to P56 ($P = 0.001$) such that the value at P56 was not significantly different from that at P0 ($P = 0.995$). λt Showed an increasing trend (but not statistically significant; $P = 0.08$) from P0 to P8 and thereafter decreased significantly (Fig. 5). The axial diffusivity showed a significant decrease between P0 and P21, but no significant changes were observed between P21 and P56 (Fig. 5). MD showed an increasing trend from P0 to P4 ($P = 0.065$) and a steady and significant decrease from P4 to P56.

The FA of both scc and gcc significantly increased between P0 and P21 but showed no further significant changes thereafter. The values of λt decreased with time ($P \leq 0.046$; P0 vs. P21) but remained the same until P56 ($P \geq 0.92$; P21 vs. P56), whereas λl did not show significant changes in both genu and splenium. MD of splenium and genu showed a behavior similar to that of the body of corpus callosum.

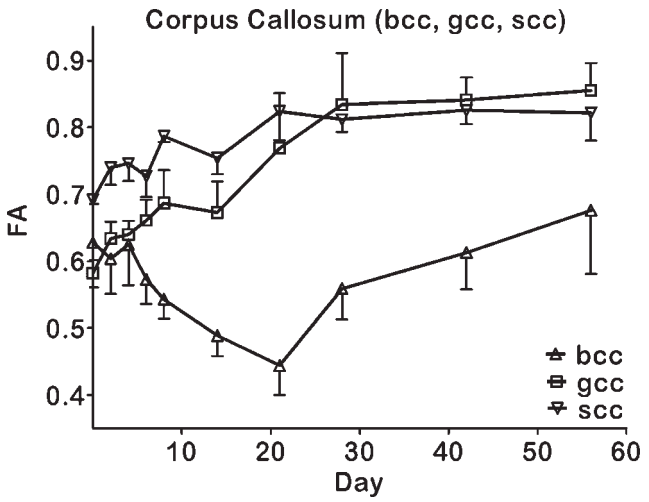

Fig. 4. Temporal changes in the FA values of three corpus callosum structures. The FA values of gcc (□) and scc (▽) significantly increased between P0 and P56. The FA value of bcc (△) significantly decreased between P0 and P21. After P21, the FA completely recovered by P56 ($P = 0.995$; P0 vs. P56 and $P = 0.001$; P21 vs. P56).

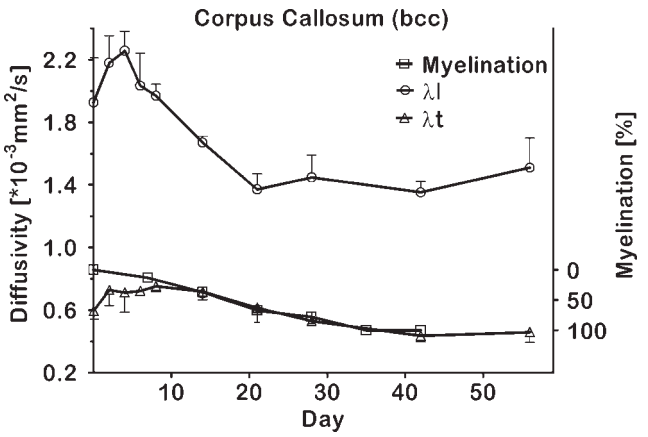

Fig. 5. Temporal changes in the axial and radial diffusivities in the body of corpus callosum (bcc) along with changes in myleination. The decrease in λl (○) between P0 and P21 appears to be the main reason for the initial decrease of the bcc's FA displayed in Figure 4, possibly indicating axonal pruning and/or apoptosis. λt (△) Appears more stabile in the initial period but decreases after P14, which might indicate the onset of myelination. Changes in λl are less prominent during this period, suggesting the end of axonal pruning and/or apoptosis. The right y-axis (reverse scaling) determines the degree of myelination (□) in percentage (P0 = 0%, P42 = 100%), evaluated by absorption spectroscopy of stained tissue extracts (Hamano et al., 1998). The remarkable similarity in the temporal pattern between myelination and λt can easily be appreciated in this figure.

External capsule. No significant variation was observed in FA from P0 to P6. Afterward, the FA significantly increased up to P28 but remained unchanged thereafter ($P = 1.00$; P28 vs. P56). λt Increased significantly between P0 and P8, followed by a significant decrease. λl Did not show significant changes between P0 and P56. MD showed temporal changes similar to those of λt.

Internal capsule, fimbria, anterior commisure, and cingulum. The temporal behavior of the DTI metrics of internal capsule, fimbria, anterior commisure, and cingulum was similar to that observed in external capsule.

DISCUSSION

We believe that these are the first quantitative studies that report in vivo postnatal development of DTI metrics in multiple structures at multiple postnatal time points in the developing rat brain. The data on normal animals in our studies should be useful in understanding the effect of brain injury on normal brain development.

Overall, our results are in good agreement with the DTI data recently obtained in mice (Guilfoyle et al., 2003; Zhang et al., 2006; Chahboune et al., 2007; Larvaron et al., 2007) and rats (Boretius et al., 2004; Sizonenko et al., 2007) but not with other published values (Xue et al., 1999; Verma et al., 2005; Lee et al., 2006; Mayer et al., 2007; Table I). Some of the reported FA values in these studies were up to 50% smaller than what we measured (Xue et al., 1999; Verma et al., 2005; Lee et al., 2006; Mayer et al., 2007; Table I). It has been shown by Landman et al. (2007) that fixation by immersion, not perfusion, could have a dramatic effect on the FA values measured ex vivo. However, the differences between our results and the published in vivo studies could be attributed, at least in part, to the methodological issues. The gradient-encoding scheme plays an important role on the estimated values of DTI metrics. The gradient-encoding scheme that we employed in these studies is balanced and rotationally invariant, which minimizes bias in estimation of the DTI metrics. In contrast, most of the studies employed six gradient directions, a scheme that is not rotationally invariant (Table I). In our studies we employed 42 gradient directions with excellent SNR, which results in reduced estimation bias (Madi et al., 2005). This, coupled with the stringent quality-control methods that we have implemented (Madi et al., 2005), resulted in accurate DTI metrics. The encoding scheme used in these studies employs alternating gradient polarities, which minimized the effect of cross terms and background gradients on the estimated FA values (Madi et al., 2005). Finally, we performed multiple ROI measurements on at least four animals at each time point.

The temporal changes in the cortical anisotropy observed in our studies are consistent with human fetal studies (McKinstry et al., 2002; Neil et al., 2002; Maas et al., 2004; Deipolyi et al., 2005; Gupta et al., 2005; Huang et al., 2006; Huppi and Dubois, 2006). In humans, cp shows a dramatic increase of FA between gestational age 100 and 200 days (FA $\sim$ 0.1 and 0.6, respectively), followed by a very steep decrease to 0.1 at day 0 (Gupta et al., 2005). In rats, the decrease in FA

occurs during the first week after birth (Fig. 2). Similar in vivo results were reported for mice by Huang et al. (2007) and for rats by Sizonenko et al. (2007).

We observed in rats a decrease in MD with age similar to that in neonates and children (Neil et al., 2002; Huppi and Dubois, 2006). The decrease was present in all structures, with the most prominent changes between P8 and P28.

We can divide the temporal dynamics of DTI metrics into four phases, based on the current study. First was a very early phase immediately after birth, between P0 and P2, in which rapid changes in the DTI metrics were observed. The second phase from P2 to about P8 did not show any dramatic changes except in cc, cp, and ec. In the third phase, from P8 to P21, all DTI metrics showed changes. In the fourth period, from P21 to P56, the DTI metrics of all structures, with the exception of the body of the corpus callosum, reached a plateau. Based on the published literature, several factors may contribute to the observed changes in the postnatal age in rats.

1. The proliferation and migration of cells in rats begin at gestational day 9.5 (G9.5) and ends at about P15 (Rice and Barone, 2000). In this phase, highly anisotropic radial glia cells support the migration of neurons from the ventricular zone to the pial surface of the cortex (Campbell and Gotz, 2002; Hatten, 1999). This, for example, should result in the high anisotropy that was observed in cp at P0 (Figs. 1, 2) and is consistent with the trend reported in human fetus (McKinstry et al., 2002; Neil et al., 2002; Maas et al., 2004; Deipolyi et al., 2005; Gupta et al., 2005; Huang et al., 2006; Huppi and Dubois, 2006). However, this period represents the end stage of neuronal proliferation/migration. As pointed out by Rakic et al. (2003) and Volpe et al. (2001), this period of neocortical maturation is associated with transition of radial glia to astrocytes and proliferation of glial cells. Consequently, one would expect a decline in the diffusion anisotropy during this period. This is consistent with our observed temporal behavior of FA in the cortical plate (Fig. 2).

In contrast to cp, the FA values in cm, cpu, and hp remain almost constant from P0 to P56. One possible explanation is that in these structures the neuronal proliferation/migration pattern is complete earlier than P0. However, we are not aware of any literature that supports this speculation.

2. Apoptosis and axonal pruning are considered a refinement of the embryonic nervous system during its development (Kantor and Kolodkin, 2003). In this period, overabundant cells, such as radial glia, experience programmed cell death, resulting in decreased tissue anisotropy. One could speculate that apoptosis and axonal pruning are responsible for the observed decrease in FA value of cp (Fig. 2). This might also be responsible for the decrease in the FA of bcc between P0 and P21 (Fig. 4), a period during which midline glia cells that support the formation of the cc are eliminated (Richards et al., 2004; Ren et al., 2006; Lindwall et al., 2007). Additionally, axonal pruning could contribute to decreased FA in the bcc. This process reduces intermingling axon branches or overabundant axons (Richards et al., 2004; Ren et al., 2006). Axonal pruning shortens the length of axons and consequently reduces the diffusivity in directions of the fibers, λl. As can be seen in Figure 5, most dominant changes in λl occur between P8 and P28.

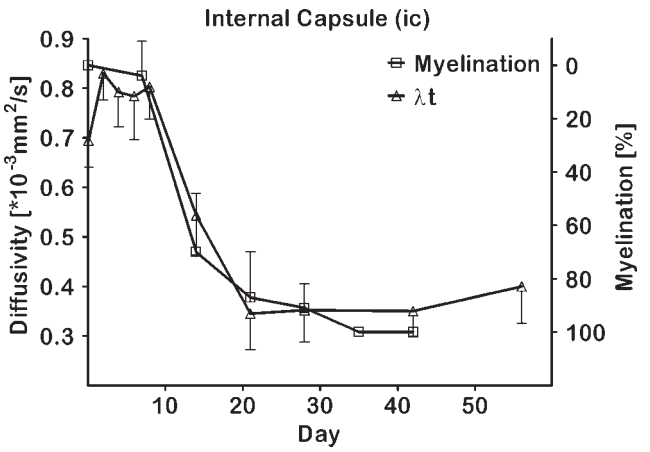

Fig. 6. Temporal changes in myelination (□) and λt (△) in the internal capsule (ic): The left y-axis refers to λt values determined in this study. The right y-axis (reverse scaling) is a measure for the degree of myelination (P0 = 0%, P42 = 100%) determined by in vitro staining techniques (Hamano et al., 1998). The remarkable similarity in the temporal pattern between myelination and λt can easily be appreciated in this figure.

3. Myelination increases the FA value (Verma et al., 2005). Myelination in rat brain starts after P10, reaches its maximum at about P20, and decreases until P45. Afterward, myelination continues at a low but constant level (Wiggins, 1986). Myelination of the cc starts after P12, reaches its maximum at about P45, and decreases until P120. The FA of cc increased from P21 (Fig. 4), consistent with Wiggins' (1986) observations. Because λt is known to be more sensitive to the state of myelination (Song et al., 2002; Deo et al., 2006), we have plotted the temporal changes in λt along with the reported myelin concentration (Hamano et al., 1998), as assessed by the myelin basic protein (MBP) staining for bcc and ic (Figs. 5,6). In these plots, the value a P0 was set to 0% and 100% myelination at P42. The remarkable similarity in the temporal variation between myelin increase and decrease in λt can be easily appreciated from these figures. This suggests that the decreased radial diffusivity from P10 is the result of myelination of these white matter structures.

4. Synaptogenesis begins in the cortex at P10 and ends at P30 (Rice and Barone, 2000), increasing the connectivity between cells. All gray matter structures showed a significant decrease in λt (except cp) and λl between P0 and P21. This matches with the measured density of synaptic junctions in the parietal cortex of rats (O'Callaghan, 1992).

To understand the observed temporal behavior of various DTI metrics, we have separated various developmental events. This is too simplistic. In reality, however, temporally the processes of proliferation and migration overlap with apopotosis and axonal pruning (Rice and Barone, 2000).

CONCLUSIONS

In summary, we have reported the temporal changes in the in vivo DTI metrics of various white and gray matter structures in Wistar rats starting from P0 to P56. We related the observed changes in DTI metrics to the known brain developmental milestones. The results of these studies are expected to provide necessary normative data that can be used to assess the effect of perinatal brain injury on normal brain development.

ACKNOWLEDGMENTS

We thank Tessy Chacko for her assistance with animal handling. Development of the DTI protocol and analysis is supported by NINDS/NIH grant R01 NS 30821 (to P.A.N.). The 7T MRI scanner is funded by NCRR/NIH grant S10 RR17205 (to P.A.N.).

REFERENCES

Arpino C, Domizio S, Carrieri MP, Brescianini DS, Sabatino MG, Curatolo P. 2001. Prenatal and perinatal determinants of neonatal seizures occurring in the first week of life. J Child Neurol 16:651–656.

Boretius S, Natt O, Watanabe T, Tammer R, Ehrenreich L, Frahm J, Michaelis T. 2004. In vivo diffusion tensor mapping of the brain of squirrel monkey, rat, and mouse using single-shot STEAM MRI. Magma 17:339–347.

Campbell K, Gotz M. 2002. Radial glia: multi-purpose cells for vertebrate brain development. Trends Neurosci 25:235–238.

Chahboune H, Ment LR, Stewart WB, Ma X, Rothman DL, Hyder F. 2007. Neurodevelopment of C57B/L6 mouse brain assessed by in vivo diffusion tensor imaging. NMR Biomed 20:375–382.

Deipolyi AR, Mukherjee P, Gill K, Henry RG, Partridge SC, Veeraraghavan S, Jin H, Lu Y, Miller SP, Ferriero DM, Vigneron DB, Barkovich AJ. 2005. Comparing microstructural and macrostructural development of the cerebral cortex in premature newborns: diffusion tensor imaging vs. cortical gyration. Neuroimage 27:579–586.

Deo AA, Grill RJ, Hasan KM, Narayana PA. 2006. In vivo serial diffusion tensor imaging of experimental spinal cord injury. J Neurosci Res 83:801–810.

Eshraghi AA, Nehme O, Polak M, He J, Alonso OF, Dietrich WD, Balkany TJ, Van De Water TR. 2005. Cochlear temperature correlates with both temporalis muscle and rectal temperatures. Application for testing the otoprotective effect of hypothermia. Acta Otolaryngol 125:922–928.

Fabian RH, Perez-Polo JR, Kent TA. 2007. A decoy oligonucleotide inhibiting nuclear factor-kappaB binding to the IgGkappaB consensus site reduces cerebral injury and apoptosis in neonatal hypoxic-ischemic encephalopathy. J Neurosci Res 85:1420–1426.

Greer RJ, Cohn LA, Dodam JR, Wagner-Mann CC, Mann FA. 2007. Comparison of three methods of temperature measurement in hypothermic, euthermic, and hyperthermic dogs. J Am Vet Med Assoc 230:1841–1848.

Guilfoyle DN, Helpern JA, Lim KO. 2003. Diffusion tensor imaging in fixed brain tissue at 7.0 T. NMR Biomed 16:77–81.

Gupta RK, Hasan KM, Trivedi R, Pradhan M, Das V, Parikh NA, Narayana PA. 2005. Diffusion tensor imaging of the developing human cerebrum. J Neurosci Res 81:172–178.

Hagberg H, Ichord R, Palmer C, Yager JY, Vannucci SJ. 2002. Animal models of developmental brain injury: relevance to human disease. A summary of the panel discussion from the Third Hershey Conference on Developmental Cerebral Blood Flow and Metabolism. Dev Neurosci 24:364–366.

Hahn K, Prigarin S, Hasan K. 2004. A novel denoising technique for very noisy DTI data. Proc Int Soc Magn Reson Med. Berkeley, CA. p 1208.

Hahn K, Prigarin S, Hasan K. 2005. The feasibility of diffusion tensor imaging for the human brain at 1 mm^3 resolution. Proc Int Soc Magn Reson Med. Berkeley, CA. p 161.

Hamano K, Takeya T, Iwasaki N, Nakayama J, Ohto T, Okada Y. 1998. A quantitative study of the progress of myelination in the rat central nervous system, using the immunohistochemical method for proteolipid protein. Brain Res Dev Brain Res 108:287–293.

Hasan KM, Alexander AL, Narayana PA. 2004. Does fractional anisotropy have better noise immunity characteristics than relative anisotropy in diffusion tensor MRI? An analytical approach. Magn Reson Med 51:413–417.

Hasan KM, Gupta RK, Santos RM, Wolinsky JS, Narayana PA. 2005. Diffusion tensor fractional anisotropy of the normal-appearing seven segments of the corpus callosum in healthy adults and relapsing-remitting multiple sclerosis patients. J Magn Reson Imag 21:735–743.

Hatten ME. 1999. Central nervous system neuronal migration. Annu Rev Neurosci 22:511–539.

Huang H, Zhang J, Wakana S, Zhang W, Ren T, Richards LJ, Yarowsky P, Donohue P, Graham E, van Zijl PC, Mori S. 2006. White and gray matter development in human fetal, newborn and pediatric brains. Neuroimage 33:27–38.

Huang H, Yamamoto A, van Zijl P, Mori S. 2007. Cortical FA mapping of developing rat brains. Proc Int Soc Magn Reson Med. Berkeley, CA. p 1616.

Huppi PS, Dubois J. 2006. Diffusion tensor imaging of brain development. Semin Fetal Neonatal Med 11:489–497.

Kamel M, Xie L-M, Xue L, Wosik J, Nesteruk K, Bockhorst K, Narayana PA. 2007. 7 Tesla very high SNR superconducting receive-only coil for rat brain imaging. Proc Int Soc Magn Reson Med. Berkeley, CA. p 327.

Kantor DB, Kolodkin AL. 2003. Curbing the excesses of youth: molecular insights into axonal pruning. Neuron 38:849–852.

Landman B, Huang H, Prince J, Ying S. 2007. A window for high-resolution post-mortem DTI: mapping contrast changes in neural degeneration. Proc Int Soc Magn Res Med. Berkeley, CA. p 1609.

Larvaron P, Boespflug-Tanguy O, Renou JP, Bonny JM. 2007. In vivo analysis of the post-natal development of normal mouse brain by DTI. NMR Biomed 20:413–421.

Lee FK, Fang MR, Antonio GE, Yeung DK, Chan ET, Zhang LH, Yew DT, Ahuja AT. 2006. Diffusion tensor imaging (DTI) of rodent brains in vivo using a 1.5T clinical MR scanner. J Magn Reson Imag 23:747–751.

Lindwall C, Fothergill T, Richards LJ. 2007. Commissure formation in the mammalian forebrain. Curr Opin Neurobiol 17:3–14.

Maas LC, Mukherjee P, Carballido-Gamio J, Veeraraghavan S, Miller SP, Partridge SC, Henry RG, Barkovich AJ, Vigneron DB. 2004. Early laminar organization of the human cerebrum demonstrated with diffusion tensor imaging in extremely premature infants. Neuroimage 22:1134–1140.

Madi S, Hasan KM, Narayana PA. 2005. Diffusion tensor imaging of in vivo and excised rat spinal cord at 7 T with an icosahedral encoding scheme. Magn Reson Med 53:118–125.

Mayer D, Zahr NM, Adalsteinsson E, Rutt B, Sullivan EV, Pfefferbaum A. 2007. In vivo fiber tracking in the rat brain on a clinical 3T MRI system using a high strength insert gradient coil. Neuroimage 35:1077–1085.

McKinstry RC, Mathur A, Miller JH, Ozcan A, Snyder AZ, Schefft GL, Almli CR, Shiran SI, Conturo TE, Neil JJ. 2002. Radial organization of developing preterm human cerebral cortex revealed by non-invasive water diffusion anisotropy MRI. Cereb Cortex 12:1237–1243.

Mori S, Zhang J. 2006. Principles of diffusion tensor imaging and its applications to basic neuroscience research. Neuron 51:527–539.

Mori S, Itoh R, Zhang J, Kaufmann WE, van Zijl PC, Solaiyappan M, Yarowsky P. 2001. Diffusion tensor imaging of the developing mouse brain. Magn Reson Med 46:18–23.

Nair G, Tanahashi Y, Low HP, Billings-Gagliardi S, Schwartz WJ, Duong TQ. 2005. Myelination and long diffusion times alter diffusion-tensor-imaging contrast in myelin-deficient shiverer mice. Neuroimage 28:165–174.

Neil J, Miller J, Mukherjee P, Huppi PS. 2002. Diffusion tensor imaging of normal and injured developing human brain—a technical review. NMR Biomed 15:543–552.

Numano T, Homma K, Iwasaki N, Hyodo K, Nitta N, Hirose T. 2006. In vivo isotropic 3D diffusion tensor mapping of the rat brain using diffusion-weighted 3D MP-RAGE MRI. Magn Reson Imag 24:287–293.

O'Callaghan J. 1992. Assessment of Neurotoxicity using assays of neuron- and glia-localized proteins: chronology and critique. In: Tilson H, Mitchel C, editors. New York: Raven Press. p 83–99.

Paxinos G, Watson C. 2005. The rat brain in stereotaxic coordinates. Amsterdam: Elsevier.

Qiao M, Meng S, Scobie K, Foniok T, Tuor UI. 2004. Magnetic resonance imaging of differential gray vs. white matter injury following a mild or moderate hypoxic-ischemic insult in neonatal rats. Neurosci Lett 368:332–336.

Rakic P. 2003. Developmental and evolutionary adaptations of cortical radial glia. Cereb Cortex 13:541–549.

Ren T, Anderson A, Shen WB, Huang H, Plachez C, Zhang J, Mori S, Kinsman SL, Richards LJ. 2006. Imaging, anatomical, and molecular analysis of callosal formation in the developing human fetal brain. Anat Rec A Discov Mol Cell Evol Biol 288:191–204.

Rice D, Barone S, Jr. 2000. Critical periods of vulnerability for the developing nervous system: evidence from humans and animal models. Environ Health Perspect 108(Suppl 3):511–533.

Rice JE 3rd, Vannucci RC, Brierley JB. 1981. The influence of immaturity on hypoxic-ischemic brain damage in the rat. Ann Neurol 9:131–141.

Richards LJ, Plachez C, Ren T. 2004. Mechanisms regulating the development of the corpus callosum and its agenesis in mouse and human. Clin Genet 66:276–289.

Sizonenko SV, Camm EJ, Garbow JR, Maier SE, Inder TE, Williams CE, Neil JJ, Huppi PS. 2007. Developmental changes and injury induced disruption of the radial organization of the cortex in the immature rat brain revealed by in vivo diffusion tensor MRI. Cereb Cortex [Feb 27 e-pub ahead of print].

Song SK, Sun SW, Ramsbottom MJ, Chang C, Russell J, Cross AH. 2002. Dysmyelination revealed through MRI as increased radial (but unchanged axial) diffusion of water. Neuroimage 17:1429–1436.

Toet MC, Groenendaal F, Osredkar D, van Huffelen AC, de Vries LS. 2005. Postneonatal epilepsy following amplitude-integrated EEG-detected neonatal seizures. Pediatr Neurol 32:241–247.

Vannucci RC, Connor JR, Mauger DT, Palmer C, Smith MB, Towfighi J, Vannucci SJ. 1999. Rat model of perinatal hypoxic-ischemic brain damage. J Neurosci Res 55:158–163.

Verma R, Mori S, Shen D, Yarowsky P, Zhang J, Davatzikos C. 2005. Spatiotemporal maturation patterns of murine brain quantified by diffusion tensor MRI and deformation-based morphometry. Proc Natl Acad Sci U S A 102:6978–6983.

Volpe JJ. 2001. Neurology of the newborn. Philadelphia: W.B. Saunders. p 57–60.

Wiggins RC. 1986. Myelination: a critical stage in development. Neurotoxicology 7:103–120.

Woods RP, Grafton ST, Holmes CJ, Cherry SR, Mazziotta JC. 1998a. Automated image registration: I. General methods and intrasubject, intramodality validation. J Comput Assist Tomogr 22:139–152.

Woods RP, Grafton ST, Watson JD, Sicotte NL, Mazziotta JC. 1998b. Automated image registration: II. Intersubject validation of linear and nonlinear models. J Comput Assist Tomogr 22:153–165.

Xue R, van Zijl PC, Crain BJ, Solaiyappan M, Mori S. 1999. In vivo three-dimensional reconstruction of rat brain axonal projections by diffusion tensor imaging. Magn Reson Med 42:1123–1127.

Zhang J, van Zijl PC, Mori S. 2002. Three-dimensional diffusion tensor magnetic resonance microimaging of adult mouse brain and hippocampus. Neuroimage 15:892–901.

Zhang J, Richards LJ, Yarowsky P, Huang H, van Zijl PC, Mori S. 2003. Three-dimensional anatomical characterization of the developing mouse brain by diffusion tensor microimaging. Neuroimage 20:1639–1648.

Zhang J, Miller MI, Plachez C, Richards LJ, Yarowsky P, van Zijl P, Mori S. 2005. Mapping postnatal mouse brain development with diffusion tensor microimaging. Neuroimage 26:1042–1051.

Zhang J, van Zijl PC, Mori S. 2006. Image contrast using the secondary and tertiary eigenvectors in diffusion tensor imaging. Magn Reson Med 55:439–449.